

Applications of a bilateral denoising filter in biological electron microscopy

Wen Jiang,^a Matthew L. Baker,^a Qiu Wu,^b Chandrajit Bajaj,^b and Wah Chiu^{a,*}

^a Verna and Marrs McLean Department of Biochemistry and Molecular Biology, Baylor College of Medicine, One Baylor Plaza, Houston, TX 77030, USA

^b Institute for Computational Engineering and Sciences, University of Texas at Austin, Austin, TX 78712, USA

Received 20 August 2003, and in revised form 17 September 2003

Abstract

Due to the sensitivity of biological sample to the radiation damage, the low dose imaging conditions used for electron microscopy result in extremely noisy images. The processes of digitization, image alignment, and 3D reconstruction also introduce additional sources of noise in the final 3D structure. In this paper, we investigate the effectiveness of a bilateral denoising filter in various biological electron microscopy applications. In contrast to the conventional low pass filters, which inevitably smooth out both noise and structural features simultaneously, we found that bilateral filter holds a distinct advantage in being capable of effectively suppressing noise without blurring the high resolution details. In as much, we have applied this technique to individual micrographs, entire 3D reconstructions, segmented proteins, and tomographic reconstructions.
© 2003 Elsevier Inc. All rights reserved.

Keywords: Bilateral filter; Denoising; Electron cryomicroscopy; Image processing; 3D reconstruction

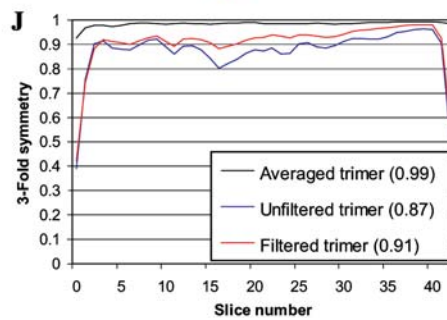
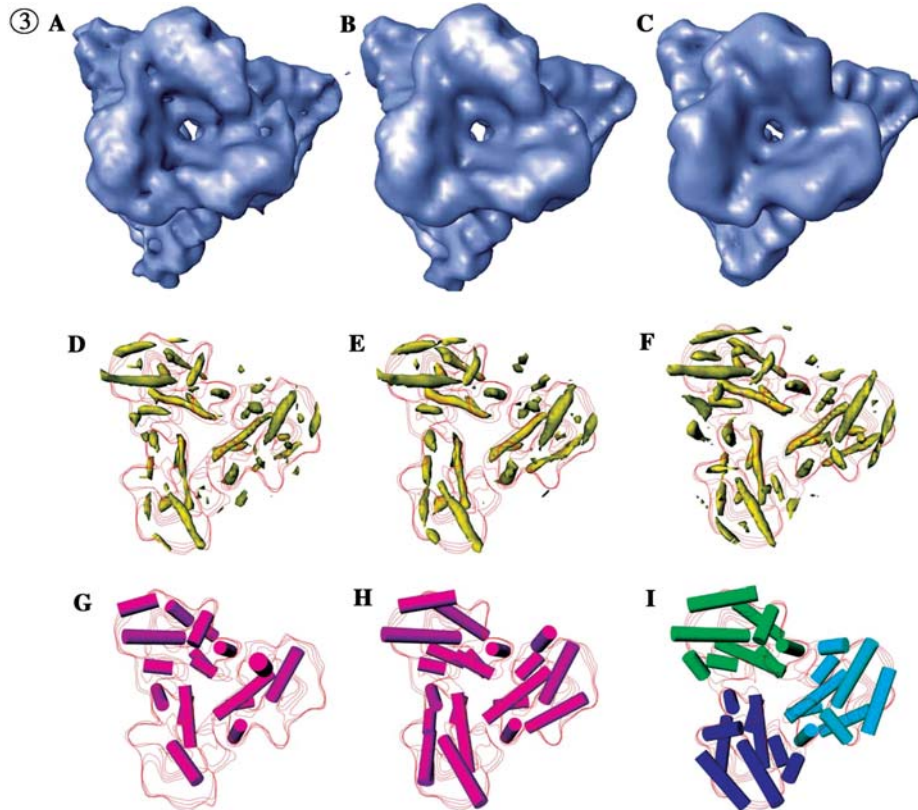
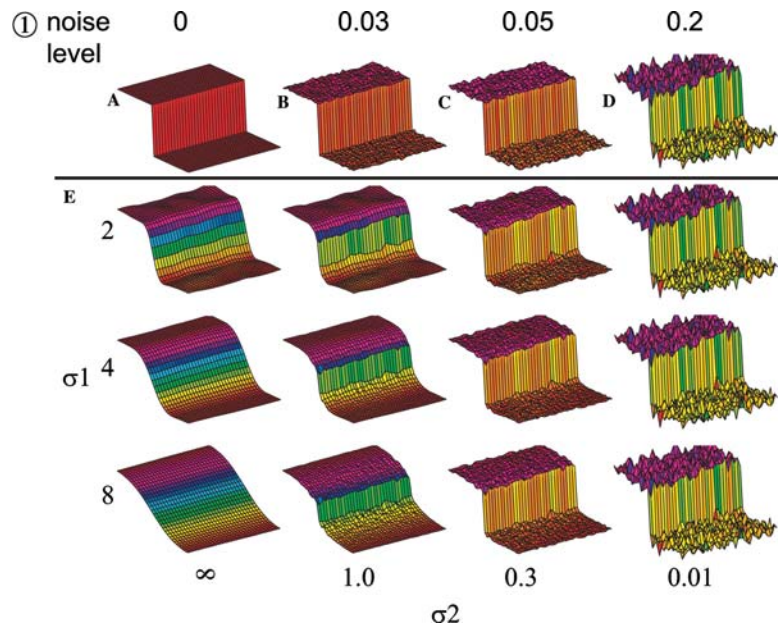
1. Introduction

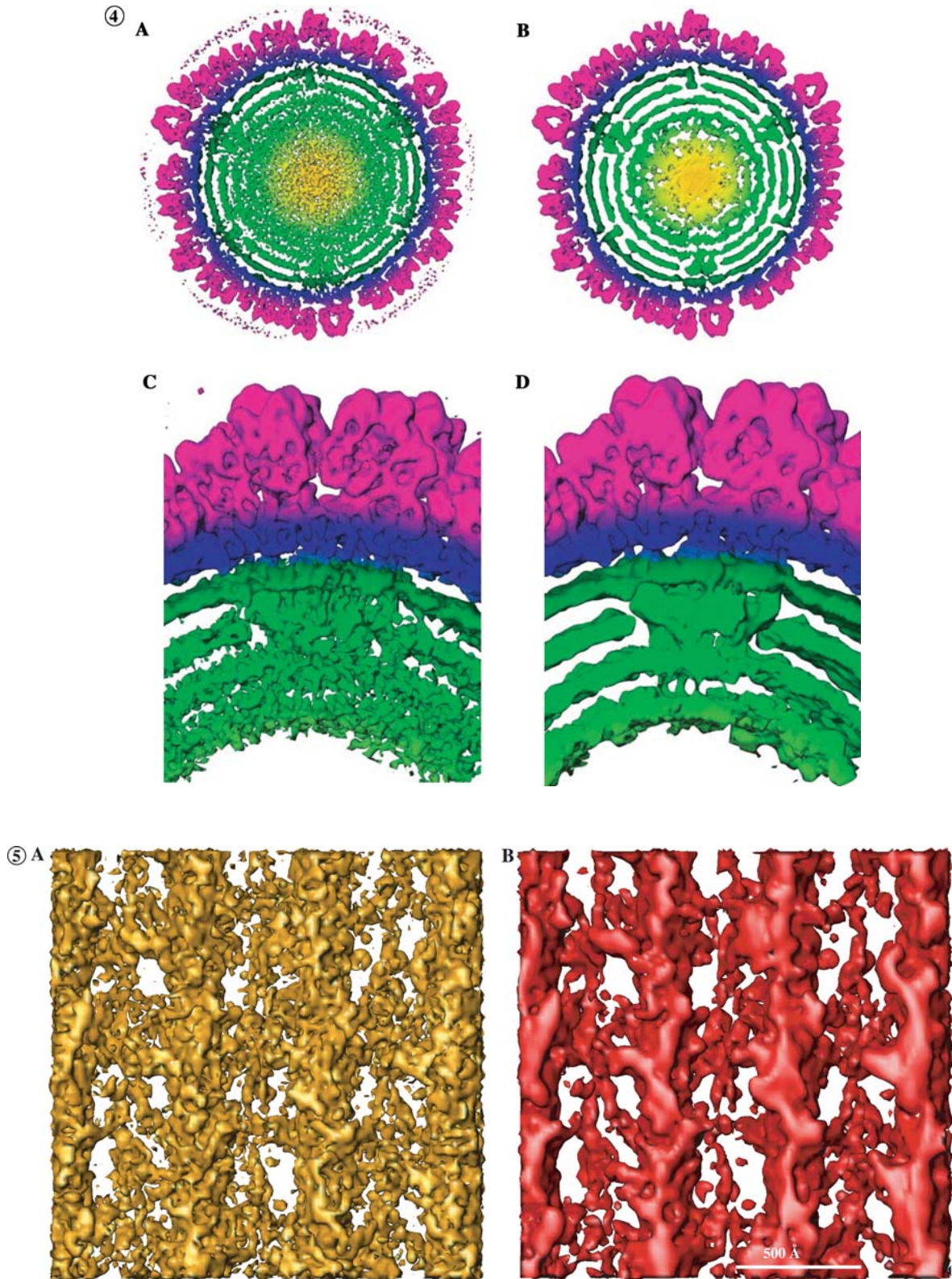
Electron cryomicroscopy is an emerging powerful technology in solving the 3D structures of large macromolecular assemblies and cellular complexes (Baumeister, 2002; Baumeister and Steven, 2000; Chiu et al., 2002; Frank, 2002; Sali et al., 2003). Due to the inherent sensitivities for biological molecules to the high energy electron radiations, imaging must be conducted using low dose conditions (Glaeser and Taylor, 1978). While low temperature at liquid nitrogen (78 K) or even liquid helium (4 K) have been employed to increase the radiation dose tolerance, the maximal allowed dose is still limited to very low levels. As a result, images are extremely noisy compared to other imaging techniques such as light microscopy, CT, and MRI. In addition, digitization noise, computational errors in image processing, and 3D reconstruction also contribute extra level of noise in the final 3D map. The image processing

procedures including particle selection, particle orientation determination, contrast transfer function correction, 3D reconstruction, and structural analysis of the reconstructions are sensitive to various levels of noise. The accuracy of these algorithms is inversely correlated to the level of noise in the data (Joyeux and Penczek, 2002). In such, it would be useful to be able to minimize the noise level in the data to improve the image processing accuracy, which will in turn improve the 3D reconstructions and structural analysis.

Many image filters have been developed to suppress the noise, such as low pass, Wavelet transforms, median filters, etc. (Gonzalez and Woods, 2002). A fundamentally important property for any filter to possess, but often lacking, is the ability to maximally suppress noise solely without affecting much of the true signal. The bilateral filter is designed to achieve this goal by striking a fine balance between minimizing noise and losing signal. The bilateral filter is a relatively new filter proposed originally to denoise 2D photographic images and has been shown to be very effective in achieving this goal (Tomasi and Manduchi, 1998). In this study, we continue to explore filtering by investigating the

* Corresponding author. Fax: 1-713-798-1625.
E-mail address: wah@bcm.tmc.edu (W. Chiu).





effectiveness of the bilateral filter in denoising biological electron microscopy images and 3D reconstructions.

The kernel of a bilateral filter is composed of an inner product of two low pass filters in real space (Tomasi and

Manduchi, 1998). The first of these filters is a normal low pass filter, which basically averages the neighboring pixel intensity values with decreasing weights for pixels at larger distances. The second one is also a type of low

Fig. 1. Illustrations of bilateral filter. (A) The step function with 0 for one half side and 1 for the other half side. (B–D) The noise-free step function in (A) was added varying levels of random noises of Gaussian distribution with the half-width at 0.03 (B), 0.05 (C), and 0.2 (D), respectively. (E) Results of bilateral filtering with combinations of varying σ_1 (2, 4, and 8 pixels half-width) and σ_2 (∞ , 1.0, 0.3, and 0.01 half-width) on the noisy step function in (D).

Fig. 3. Bilateral filtering of 3D reconstructions for secondary structure identification. (A) A single, unaveraged P8 trimer from the 6.8 Å RDV reconstruction. (B) The same P8 trimer filtered with $\sigma_1 = 4$ and $\sigma_2 = 4$. (C) The average RDV P8 trimer as published by Zhou et al. (D–F) Intermediate cross-correlation map (yellow) from *helixhunter* of the unfiltered (D), filtered, (E) and average (F) P8 trimer indicating potential helices. (G–I) Final *helixhunter* determined helices for the P8 trimer from the unfiltered (G), filtered (H), and averaged (I) density map. Helices for each monomer of P8 in the averaged trimer are colored. The red lines in (D–I) indicate basic shape of the P8 trimer. (J) Plot of relative 3-fold symmetry at different planes along the local 3-fold axis for each of the three trimers. The average 3-fold symmetry for all planes in each trimer is shown in the figure legend.

Fig. 4. Bilateral filtering of 3D reconstructions for visualization. (A) Unfiltered medial slice from the 6.8 Å reconstruction of RDV. (B) Bilateral filtered image of (A) with $\sigma_1 = 3$ pixels and $\sigma_2 = 3$. (C and D) A zoomed-in view of the density at the 5-fold vertices in both the unfiltered (C) and filtered density (D) maps. Interrupting the concentric rings of RNA is a density that corresponds to the RNA-dependent RNA polymerase complex located at all of the 5-fold vertices in RDV. The iso-surface shown in (C, 0.8) and (D, 0.4) represents a contour level at which the maximal amount of density can be seen at the 5-fold vertices while still being able to resolve at least three layers of RNA.

Fig. 5. Bilateral filtering of tomogram. (A) Surface view of the original density map of tomography reconstruction of rigor flight muscle thin section. The resolution is in the range of 40–70 Å with sampling of 15.5 Å/pixel. The map density variance is 48. (B) The bilateral filtered density map (A) with $\sigma_1 = 1$ pixel and $\sigma_2 = 200$.

pass filter, except the weights for the neighboring pixels are derived from the pixel intensity value differences to the center pixel intensity value instead of geometric distances. Therefore, the larger the pixel value difference, the smaller the pixels contribution during averaging. This second filter component distinguishes the bilateral filter and results in a significant advantage over other types of filters. In practice, both filter components in bilateral filter are realized using Gaussian functions:

$$I_{\text{out}}(\vec{r}) = \int \exp \left\{ -\frac{|\vec{\xi} - \vec{r}|^2}{2\sigma_1^2} \right\} \exp \left\{ -\frac{|I_{\text{in}}(\vec{\xi}) - I_{\text{in}}(\vec{r})|^2}{2\sigma_2^2} \right\} \times I_{\text{in}}(\vec{\xi}) d\vec{\xi}$$

where $I_{\text{in}}(\vec{r})$ is the input noisy image, $I_{\text{out}}(\vec{r})$ is the output denoised image, $\exp\{-|\vec{\xi} - \vec{r}|^2/2\sigma_1^2\} \exp\{-|I_{\text{in}}(\vec{\xi}) - I_{\text{in}}(\vec{r})|^2/2\sigma_2^2\}$ is the bilateral filter kernel, where σ_1 and σ_2 control the width of the two Gaussian functions, respectively. σ_1 controls the extent of the normal spatial low pass filtering where a larger σ_1 causes severe smoothing. σ_2 controls the discrimination power between true features and noises with the assumption that larger pixel intensity value variations are mainly from true features and smaller pixel intensity value variations are contributed by noise. In the above equation, the normalization factor is ignored. To keep the local mean, the weights $\exp\{-|\vec{\xi} - \vec{r}|^2/2\sigma_1^2\} \exp\{-|I_{\text{in}}(\vec{\xi}) - I_{\text{in}}(\vec{r})|^2/2\sigma_2^2\}$ should be normalized by the sum of all the weights $\int \exp\{-|\vec{\xi} - \vec{r}|^2/2\sigma_1^2\} \exp\{-|I_{\text{in}}(\vec{\xi}) - I_{\text{in}}(\vec{r})|^2/2\sigma_2^2\} d\vec{\xi}$.

The advantages of the bilateral filter can be illustrated using the example of “smoothing without edge blurring” shown in Fig. 1. If the noisy function is a step function (Fig. 1A) with noise (Figs. 1B–D), a normal low pass filter will suppress noise but blur the edges, with more severe blurring caused by wider Gaussian half-widths σ_1 (Fig. 1E, $\sigma_2 = \infty$ column). In contrast, the bilateral filter is capable of smoothing out the noise in the plateau regions while maintaining sharp edges (Fig. 1E, $\sigma_2 = 0.3$

column). In the plateau regions, the pixel intensity value differences from noises are much smaller than the appropriately chosen σ_2 , thus the second low pass component in bilateral filter will be close to 1.0. This results in making the bilateral filter effectively equivalent to normal low pass filters, capable of smoothing out the noise. However, when the pixels at the edge are filtered, the intensity value differences of neighboring pixels in the plateau regions are significantly larger than σ_2 , and thus cause the second component in bilateral filter to approach 0.0. This essentially cancels the contributions for those pixels and minimizes the blurring effects found in low pass filters. When σ_2 is chosen inappropriately, the bilateral filtering is similar to normal low pass filter for too large σ_2 (Fig. 1E, $\sigma_2 = 1.0$ column), or no filtering for too small σ_2 (Fig. 1E, $\sigma_2 = 0.01$ column). When σ_2 is infinite, the bilateral filter is reduced to a normal low pass filter (Fig. 1E, $\sigma_2 = \infty$ column). It is worth noting that bilateral filter is not very effective against “singular” type noise which have a single or a few noise pixels with very different values than the rest pixels. Median filter are more effective for this type of noises (Gonzalez and Woods, 2002).

2. Methods

2.1. Implementation of bilateral filter

The bilateral filter was originally implemented in C in the Center for Computational Visualization, University of Texas at Austin. This implementation was later integrated as a C++ class method for the main class, *EMData*, in the single particle image processing software suite, EMAN (Ludtke et al., 1999) developed in the National Center for Macromolecular Image, Baylor College of Medicine. Both 2D images and 3D maps are supported. The filter is exposed to the user in the

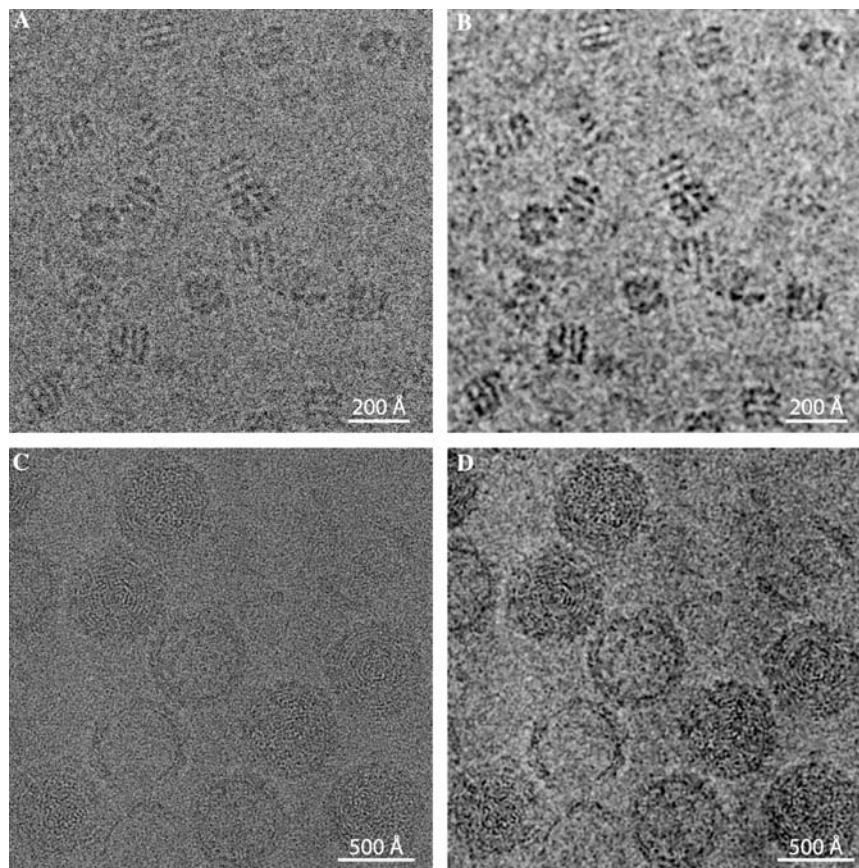


Fig. 2. Bilateral filtering of raw micrograph. (A) The original micrograph of GroEL imaged on a JEOL4000 microscope at 400 kV and 50 000 magnification. The density variance of the whole micrograph is 0.22. (B) The bilateral filtered image of (A) with $\sigma_1 = 2$ pixels and $\sigma_2 = 1.1$. (C) The original micrograph of RDV imaged on a JEOL4000 microscope at 400 kV and 50 000 magnification. (D) The bilateral filtered image of (C) with $\sigma_1 = 3$ pixels and $\sigma_2 = 5$.

multi-function programs *proc2d* for 2D images and *proc3d* for 3D maps.

Since the second component of bilateral filter is dependent on the local density distribution, the bilateral filter is a type of non-linear filter. This has prevented the use of the fast Fourier transform in accelerating the computation as normally done with the linear filters, such as normal low pass filter (Press et al., 1994). We have thus implemented the bilateral filter using a straightforward, real space convolution method. This real space implementation scales poorly with image size and kernel width. To overcome the slow speed problem for large images and maps, we also have provided a program called *bilateral-FilterP*, which is a parallelized version of the bilateral filter using the message passing interface (MPI) standard. The parallelization was done by splitting the image pixel array into small pieces with partial overlapping at the borders. The individual pieces are processed independently by different processors and the results are then pooled together in the end. The splitting is done along the sections (Z axis) for 3D maps and rows (Y axis) for 2D images.

All these implementations are cross-platform portable and work on both shared memory systems (SGI

systems) and distributed memory systems (Linux clusters). These programs are freely available in the form of binary executables and source code as part of EMAN distribution from the National Center for Macromolecular Imaging Web site (<http://ncmi.bcm.tmc.edu>). The original C implementation is also available from the Center for Computational Visualization Web Site (<http://www.ices.utexas.edu/ccv/software>).

2.2. Testing the bilateral filter

The implementation of the bilateral filter was tested on multiple types of images and maps: raw micrographs, 3D reconstruction maps of sub-nanometer resolution single particles, individual segmented proteins, and low resolution tomograms. The filtering was targeted at visual enhancement for 2D micrographs and 3D reconstructions and at secondary structural elements identification for sub-nanometer resolution 3D reconstructions. As discussed in Section 1, the bilateral filter has two free variables that the user needs to choose, σ_1 and σ_2 . The choice of these two parameters was guided by prior knowledge of the image, such as feature size of

a typical helix, sampling (Angstrom/pixel), and pixel value variance. The actual tests were performed for an array of these two parameters using these guides to find the best combination of σ_1 and σ_2 .

3. Results

3.1. Denoising micrographs

GroEL is an 800 kDa molecular chaperone which promotes protein folding in the bacterial cell. The GroEL particles were imaged on a JEOL4000 electron cryomicroscope at 400 kV and 50 K magnification. The micrographs were scanned using a Zeiss SCAI flatbed scanner at 7 μm step size and were later averaged to 14 μm step size. This resulted in a 11.5 Å resolution 3D reconstruction using the EMAN software (Ludtke et al., 2001). Shown in Fig. 2A is a micrograph at 2.4 μm under-focus. In the original unfiltered image, the GroEL particles are barely visible in the high noise background. However, the contrast between the particles and noise background is significantly enhanced in the bilateral filtered image (Fig. 2B). The GroEL particles are much more readily recognizable. Furthermore, the smoothing of the noise is not at the expense of blurring the particle image details. The detailed features of GroEL particle, i.e., the striations in the side views and the empty-ring in the top view, are still maintained.

Currently, rice dwarf virus (RDV) is the highest resolution (6.8 Å) virus structure (EBI-EMDB Access Code pending) determined by electron cryomicroscopy (Zhou et al., 2001). The RDV particles were imaged on a JEOL4000 electron cryomicroscope at 400 kV and 50 K magnification. The micrographs were scanned using a Zeiss SCAI flatbed scanner at 7 μm step size and were later averaged to 14 μm step size. Shown in Fig. 2C is a micrograph at 1.7 μm under-focus. As with GroEL, the RDV particles in the unfiltered image are barely visible in the high noise background. Again, the contrast between the particles and background is significantly enhanced after bilateral filtering (Fig. 2D). The characteristic RNA fingerprint is clearly visible in the filtered images.

3.2. Denoising 3D reconstructions for secondary structure analysis

In RDV, the segmented RNA genome of RDV is encapsulated by two concentric protein layers. P8 makes up a $T = 13$ outer capsid layer, while P3 makes up a $T = 1$ inner capsid layer. *Helixhunter* and *foldhunter* (Jiang et al., 2001) were used to identify α helices and localize homologous folds in both P3 and P8, resulting in pseudo-atomic models for each of the proteins (Zhou et al., 2001).

However, the densities corresponding to the dsRNA and RNA polymerase beneath the inner capsid layer were not well resolved at any isosurface contour level.

As mentioned above, identification of α helices in sub-nanometer resolution structures was effectively shown in RDV, as well as other sub-nanometer resolution structures, using *helixhunter*. In brief, *helixhunter* performs a cross-correlation between the map and a prototypical helix, followed by a segmentation and feature extraction step. While *helixhunter* represents a significant advance in feature identification, the computational identification of helices still requires a good map and user intervention for refinement of helix length and position. To decrease the reliance of such analysis on human intervention, bilateral filtering has been applied on the aforementioned RDV data set before running *helixhunter*.

In the published structure of RDV P8, four of the P8 trimers in an asymmetric unit were aligned and averaged together to enhance the density map for structural analysis. However, not all assemblies will have additional internal symmetry to allow for the averaging of multiple subunits to enhance the structural features. Shown in Fig. 3 is a single unaveraged, unfiltered P8 trimer (A), filtered P8 trimer (B), and an averaged trimer (C). Before all three P8 trimers were subjected to structural analysis using *helixhunter*, each of the three trimers was assessed for their local 3-fold symmetry using the program *symAxisSearch* in EMAN (Fig. 3J) (He et al., 2001). An increase in relative 3-fold symmetry (unfiltered: 0.87 and filtered: 0.91) is seen in the filtered data over the unfiltered data. Compared to the averaged trimer, where the 3-fold symmetry is 0.99, the increase in the extent of 3-fold symmetry in the filtered trimer likely represents the removal of noise.

In the secondary structure analysis of the P8 trimer with *helixhunter*, the intermediate correlation map in the filtered map (Fig. 3E) contains better helix-like density with far less noise than when compared to the unfiltered data (Fig. 3D). In general, the intermediate correlation map from the filtered trimer resembles that of the averaged trimer (Fig. 3F). Figs. 3G and H represent the first iteration of helix identification using *helixhunter*, while Fig. 3I represents the final helix model after multiple refinements of helix location and orientation from the average trimer. While neither of the two final *helixhunter* results (Figs. 3G and H) identifies the complete set of helices in the P8 trimer (Fig. 3I), the filtered data are far superior to the unfiltered results in the first iteration of helix identification. The helices from the filtered results are roughly 3-fold symmetric and match greater than 75% of the helices (21 of 27) identified from the average trimer with no false positives. Such analysis represents the ability of bilateral filter to remove noise and enhance structural features without over-smoothing.

3.3. Denoising 3D reconstructions for visualization

In analyzing the RDV P8 trimer, it has been shown that the bilateral filter is effective at removing noise without diminishing the high resolution secondary structure features of a density map. Even with a 6.8 Å resolution structure of RDV (3-fold medial slice shown in Fig. 4A), it has not yet been possible to effectively visualize the less-ordered dsRNA and RNA polymerase. Located at the 5-fold vertices, a RNA-dependent RNA polymerase is responsible for transcribing the RNA genome (Fig. 4C), which is organized as “coned-coils” inside the capsid (Pesavento et al., 2001). The bilateral filter was applied to the entire 6.8 Å map of RDV in order to enhance visualization of these components

After applying the bilateral filter to the RDV reconstruction, both the viral RNA and RNA polymerase complex, features that were only partially visible in the unfiltered map, became visible. The characteristic RNA fingerprint pattern in a cross-sectional slice was clearly visible after filtering (Fig. 4B). After more closely examining the RNA density, the rings of genomic RNA can be seen, interrupted at the 5-fold axis by the density likely corresponding to the RNA polymerase (Fig. 4D). Additionally, the filtered map also shows nearly identical features of the capsid proteins as the unfiltered RDV reconstruction. In such, the bilateral filter appears to have specifically removed noise while maintaining the fine structural features.

3.4. Denoising tomograms

We have tested the bilateral filter on an electron tomography reconstruction of actomyosin structures from the thin section of rigor insect flight muscle (Chen et al., 2002). The density map was retrieved from the publicly available EM density map archive (EBI-EMDB Access Code: EMD-1001). In Fig. 5, the surface view of the central block (100 × 100 × 20 pixels) of the density map is shown for the originally deposited (Fig. 5A) and the bilateral filtered map (Fig. 5B, $\sigma_1 = 1$ pixel and $\sigma_2 = 200.0$). In the unfiltered image, there are significant levels of residual noise, making the thin actin filaments between the thick myosin filaments hard to see. In the filtered image, however, the noise is significantly reduced and the thin actin filaments and the myosin head cross-bridges are much more clearly visualized.

4. Discussions

For electron cryomicroscopy of single particles, the first step in image processing is to locate and box out the individual particles from the raw micrograph scans or CCD images. The high level of noise and low contrast make it hard to distinguish particles from the back-

ground. This not only makes human interactive particle selection painful but also has allowed for only limited success in automated particle picking methods (Nicholson and Glaeser, 2001). By applying the bilateral filter, we have shown that the noise in the raw micrograph can be significantly smoothed out, while the contrast between the particle and the background is significantly enhanced. The enhanced contrast allows the user to distinguish good particles from noise much more readily and improve the speed of particle selection. It is also reasonable to expect that the denoised micrographs will be beneficial in improving automated particle picking procedures.

In achieving high resolution structures of macromolecular complexes, the ability to discern the molecular components and their structural features is paramount to the overall understanding of the macromolecule function. In such, one of the most critical aspects of structure determination is visualization. Sub-nanometer reconstructions often contain significant amounts of noise as well as unordered and/or missing density. By low pass filtering such data, visual and computational analysis of the structures can be improved, generally at the cost of the resolvability of the map. In applying the aforementioned bilateral filter to electron cryomicroscopy density maps, such problems may be avoided. The resulting enhanced image allows for improved visual and computational analysis and annotation.

Electron tomography is a subfield of electron microscopy that is particularly powerful in studying cellular level structural features. Unfortunately, electron tomographic 3D reconstructions of cellular materials often do not have the repetitive structures to perform averaging as done in single particle electron cryomicroscopy. As a result, the 3D tomograms are limited to lower resolutions and are generally noisier. It is common practice to apply some denoising procedures, such as mean curvature flow (Bohm et al., 2000), non-linear anisotropic diffusion (Frangakis and Hegerl, 2001), and Wavelet transform (Stoschek and Hegerl, 1997), to the tomograms before further segmentation and analysis. We have shown here that bilateral filter is another plausible denoising method that can greatly suppress the noise in a tomogram, resulting in a better analysis of 3D tomograms. It will be useful to have further systematic comparisons between these approaches to identify the best applicable option for different types of data.

We have shown the successful application of the bilateral filter in several areas of image processing in biological electron microscopy. The tests are so far limited to only isolated steps in the complete image processing procedure, which roughly consists of particle selection, particle orientation refinement, 3D reconstruction, and 3D structural post-analysis. Particularly, bilateral filtering has not been investigated for its effects on the particle orientation refinement and 3D reconstruction.

The major problem for applying bilateral filter in the complete image refinement and 3D reconstruction process is the difficulty to choose optimal parameters (σ_1 and σ_2) for the particle images of vastly different contrast when taken at different defocuses.

The bilateral filter, however, is not without some potential artifacts. The bilateral filter is a non-linear type filter and the filtering effects are different for different images, making it very hard to characterize the aggregate effects when differently filtered images are merged into a single 3D reconstruction. It is also very difficult to “undo” the filtering for this non-linear bilateral filter, unlike other linear filters which can be perfectly undone as long as the filter does not have strict zero components. The choice of the two parameters, σ_1 and σ_2 , might also present potential problems since the current selection method for these values is dependent on a trial and error approach. Inappropriate choice of the two parameters may result not only in non-optimal filtering of noise but also over-smoothing of true features. More rational criteria for the choice of these two parameters would be necessary to make the bilateral filter more user-friendly.

Some other filters, such as Wavelet transform and anisotropic diffusion (Perona and Malik, 1990), have been advocated in recent years to also possess the property of “smoothing noise without blurring edges”. We have employed the Wavelet transform to denoise virus particles and have seen significant improvement in the orientation determination robustness for the low contrast particle images (Saad and Chiu, 2000). It has been found that anisotropic diffusion and bilateral filter are actually intimately related to each other despite differences in their mathematical expression (Bajaj and Xu, 2003; Bajaj et al., 2003; Barash, 2002). The bilateral filter is in a relatively simple form, from which it is relatively easy to understand and implement. The anisotropic diffusion filter is in a more complicated, iterative form that is harder to understand and implement; nevertheless it adds flexibility to adapt to different filtering requirements. Application of these filters to biological electron microscopy and systematic comparison of these filters with bilateral filter would be required to identify their relative advantages and disadvantages for the many different types of tasks in biological electron microscopy.

5. Conclusion

We have provided the computational framework for integrating and applying the bilateral filter to biological electron microscopy data. We have demonstrated that bilateral filtering is capable of suppressing noise while preserving high resolution secondary structure features simultaneously. Based on the four tests, the application

of the bilateral filter has significantly enhanced visualization in raw and processed images. With relatively intuitive parameters, the bilateral filter may become a useful component in extracting structural features from low dose electron microscopic data.

Acknowledgments

We thank Joanita Jakana for providing the GroEL and RDV micrographs, Dr. Z.H. Zhou for providing the RDV map, and Dr. K. Taylor for making the muscle tomogram map available in the EBI-EMDB. This research is funded by grants from NIH (P41RR02250, R21AI053737), Agouron Institute (W.C. and W.J.), NLM (T15LM07093) through the Keck Center for Computational Biology, Gulf Coast Consortia (M.B.) and NSF NPACI (C.B. and W.C.).

References

- Bajaj, C., Wu, Q., Xu, G., 2003. Level-set based volumetric anisotropic diffusion for 3D image denoising. ICES Technical Report #301, University of Texas at Austin.
- Bajaj, C., Xu, G., 2003. Anisotropic diffusion of subdivision surfaces and functions on surfaces. *ACM Trans. Graphics* 22, 4–32.
- Barash, D., 2002. A fundamental relationship between bilateral filtering, adaptive smoothing, and the nonlinear diffusion equation. *IEEE Trans. Pattern Anal. Machine Intelligence* 24, 844–847.
- Baumeister, W., Steven, A.C., 2000. Macromolecular electron microscopy in the era of structural genomics. *Trends Biochem. Sci.* 25, 624–631.
- Baumeister, W., 2002. Electron tomography: towards visualizing the molecular organization of the cytoplasm. *Curr. Opin. Struct. Biol.* 12, 679–684.
- Bohm, J., Frangakis, A.S., Hegerl, R., Nickell, S., Typke, D., Baumeister, W., 2000. Toward detecting and identifying macromolecules in a cellular context: template matching applied to electron tomograms. *Proc. Natl. Acad. Sci. USA* 97, 14245–14250.
- Chen, L.F., Winkler, H., Reedy, M.K., Reedy, M.C., Taylor, K.A., 2002. Molecular modeling of averaged rigor crossbridges from tomograms of insect flight muscle. *J. Struct. Biol.* 138, 92–104.
- Chiu, W., Baker, M.L., Jiang, W., Zhou, Z.H., 2002. Deriving folds of macromolecular complexes through electron cryomicroscopy and bioinformatics approaches. *Curr. Opin. Struct. Biol.* 12, 263–269.
- Frangakis, A.S., Hegerl, R., 2001. Noise reduction in electron tomographic reconstructions using nonlinear anisotropic diffusion. *J. Struct. Biol.* 135, 239–250.
- Frank, J., 2002. Single-particle imaging of macromolecules by cryo-electron microscopy. *Annu. Rev. Biophys. Biomol. Struct.* 31, 303–319.
- Glaeser, R.M., Taylor, K.A., 1978. Radiation damage relative to transmission electron microscopy of biological specimens at low temperature: a review. *J. Microsc.* 112, 127–138.
- Gonzalez, R.C., Woods, R.E., 2002. *Digital Image Processing*, second ed. Prentice Hall, Upper Saddle River, NJ.
- He, J., Schmid, M.F., Zhou, Z.H., Rixon, F., Chiu, W., 2001. Finding and using local symmetry in identifying lower domain movements in hexon subunits of the herpes simplex virus type1 capsid. *J. Mol. Biol.* 309, 903–914.

- Jiang, W., Baker, M.L., Ludtke, S.J., Chiu, W., 2001. Bridging the information gap: computational tools for intermediate resolution structure interpretation. *J. Mol. Biol.* 308, 1033–1044.
- Joyeux, L., Penczek, P.A., 2002. Efficiency of 2D alignment methods. *Ultramicroscopy* 92, 33–46.
- Ludtke, S.J., Baldwin, P.R., Chiu, W., 1999. EMAN: Semi-automated software for high resolution single particle reconstructions. *J. Struct. Biol.* 128, 82–97.
- Ludtke, S.J., Jakana, J., Song, J.-L., Chuang, D., Chiu, W., 2001. A 11.5 Å single particle reconstruction of GroEL using EMAN. *J. Mol. Biol.* 314, 253–262.
- Nicholson, W.V., Glaeser, R.M., 2001. Review: automatic particle detection in electron microscopy. *J. Struct. Biol.* 133, 90–101.
- Perona, P., Malik, J., 1990. Scale-space and edge detection using anisotropic diffusion. *IEEE Trans. Pattern Anal. Machine Intelligence* 12, 629–639.
- Pesavento, J.B., Lawton, J.A., Estes, M.E., Venkataram Prasad, B.V., 2001. The reversible condensation and expansion of the rotavirus genome. *Proc. Natl. Acad. Sci. USA* 98, 1381–1386.
- Press, W.H., Teukolsky, S.A., Vetterling, W.T., Flannery, B.P., 1994. *Numerical Recipes in C*, second ed. Cambridge University Press, New York.
- Saad, A., Chiu, W., 2000. Hierarchical wavelet projection matching for orientation determination of low contrast electron cryomicroscopic images of icosahedral virus particles. *Int. Conf. Acoustics, Speech Signal Process.* 3, 286–290.
- Sali, A., Glaeser, R., Earnest, T., Baumeister, W., 2003. From words to literature in structural proteomics. *Nature* 422, 216–225.
- Stoschek, A., Hegerl, R., 1997. Denoising of electron tomographic reconstructions using multiscale transformations. *J. Struct. Biol.* 120, 257–265.
- Tomasi, C., Manduchi, R., 1998. Bilateral filtering for gray and color images. In: *Proceedings of the IEEE International Conference on Computer Vision*, Bombay, India, pp. 59–66.
- Zhou, Z.H., Baker, M.L., Jiang, W., Dougherty, M., Jakana, J., Dong, G., Lu, G., Chiu, W., 2001. Electron cryomicroscopy and bioinformatics suggest protein fold models for rice dwarf virus. *Nat. Struct. Biol.* 8, 868–873.